Geoscientific
Model Development
Discussions

1 **An interactive ocean surface albedo scheme: formulation and evaluation in**

2 **two atmospheric models**

3

4 **Roland Séférian[1*], Sunghye Baek[2,3], Olivier Boucher[2], Jean-Louis Dufresne[4], Bertrand**

5 **Decharme[1], David Saint-Martin[1], Romain Roehrig[1]**

6 [1] Centre National de Recherches Météorologiques, Météo-France/CNRS, Toulouse, France

7 [2] Institut Pierre-Simon Laplace, CNRS / UPMC, Paris, France

8 [3] Now at Korea Institute of Atmospheric Prediction Systems (KIAPS), Seoul, Korea

9 [4] Laboratoire de Météorologie Dynamique, CNRS / UPMC, Paris, France

10

11 **Abstract**

12

13 Ocean surface represents roughly 70% of the Earth surface, playing a large role in the

14 partitioning of the energy flow within the climate system. The ocean surface albedo (OSA) is

15 an important parameter in this partitioning because it governs the amount of energy

16 penetrating into the ocean or reflected towards space. The old OSA schemes in the ARPEGE

17 and LMDZ models only resolve the latitudinal dependence in an *ad hoc* way without an

18 accurate representation of the solar zenith angle dependence. Here, we propose a new

19 interactive OSA scheme suited for Earth system models, which gather contributions for

20 relevant OSA processes published in the literature over the last decades. This scheme resolves

21 spectrally the various contributions of the surface for direct and diffuse solar radiation. The

22 implementation of this scheme in two Earth system models leads to substantial improvements

23 in simulated OSA. At the local scale, models using the interactive OSA scheme better

24 replicate the day-to-day distribution of OSA derived from ground-based observations in

25 contrast to old schemes. At global scale, the improved representation of OSA for diffuse

26 radiation reduces model biases by up to 80% over the tropical oceans, reducing annual-mean

27 model-data error in surface upwelling shortwave radiation by up to 7 W m^{-2} over this domain.

28 The spatial correlation coefficient between modelled and observed OSA at monthly resolution

29 has been increased from 0.1 to 0.8. Despite its complexity, this interactive OSA scheme is

30   computationally efficient to enable precise OSA calculation without penalizing the model

31   elapsed time.

32

33

34   **1- Introduction**

35   The surface radiation budget has long been recognized as fundamental to our understanding of

36   the climate system (IPCC, 2001; 2007; 2013). The flow of radiative energy through the Earth

37   System and the radiative interactions between the atmosphere and the ocean remain one of the

38   major sources of uncertainties in climate predictions (Allen et al., 2009; Frölicher, 2016;

39   Gillett et al., 2013; Myhre et al., 2015; Otto et al., 2013).

40

41   In the atmosphere, the spatiotemporal variations in incoming solar radiation and its

42   atmospheric absorption drive the hydrological cycle as well as the flow of air masses. In the

43   oceans, the fraction of solar radiation entering in subsurface is controlled by the oceanic

44   surface albedo (OSA). The corresponding amount of heat stored into the ocean constitutes an

45   important term in the ocean energy surface balance and affects in turn the whole climate

46   system. On short (daily to seasonal) time scales, solar radiation absorbed into the upper-ocean

47   layers affects the stability of the ocean mixed layer, the sea surface temperature and may, in

48   turn, influence the geographic structure of large-scale atmospheric convection (Gupta et al.,

49   1999). Over longer time scales, the fraction of energy entering into the ocean contributes to

50   increase the ocean heat content, which is key term to diagnose the climate sensitivity from

51   observations (Otto et al., 2013).

52

53   OSA interacts with a multitude of biophysical processes occurring in the first meters of the

54   ocean. In particular, it governs the amount of solar radiation entering in the upper-most layer

55   of the ocean that interacts with marine biological light-sensitive pigment like chlorophyll, and

56   other materials in suspension (e.g., Morel and Antoine, 1994; Murtugudde et al., 2002). OSA

57   also influences a number of biogeochemical processes such as the photosynthesis, which is

58   directly related to the amount of solar radiation available within the upper-lit layer of the

59   ocean. Conversely, penetrating ultraviolet solar radiation can also produce detrimental

60   impacts on the marine biota (e.g., Li et al., 2014; Smyth, 2011). Consequently, OSA

61   influences marine primary productivity directly, and hence ocean ecosystems and ocean

62   carbon uptake (e.g., Behrenfeld and Falkowski, 1997; Nelson and Smith, 1991; Siegel et al.,

63   2002).

64

65

66 Despite its importance, OSA is a parameter that often receives insufficient attention from both

67 observational and modelling points of view. Most of the available data are indirectly retrieved

68 from satellite observations of the top-of-atmosphere radiative budget (Wielicki et al., 1996),

69 with relatively few direct observations of surface radiative fluxes. Nonetheless, the OSA

70 processes are relatively well understood so that OSA can be parameterized at the global scale.

71

72 Both empirical and theoretical approaches indicate that the solar zenith angle (SZA) is the

73 single most prominent driving parameter for OSA. However a wide range of other parameters

74 such as the partitioning of incoming solar radiation between its direct and diffuse components,

75 the sea surface state (often approximated through the surface wind), the concentration of

76 suspended matter and plankton light-sensitive pigment in the surface ocean, and the extent

77 and physical properties of whitecaps also affect OSA. All of these contributions vary

78 spectrally and OSA thus depends on the spectral distribution of the incoming solar radiation at

79 the surface (Jin, 2004; Jin et al., 2002).

80

81 Over the last decades, several schemes have been proposed to model OSA (e.g., Cox and

82 Munk, 1954; Hansen et al., 1983; Kent et al., 1996; Larsen and Barkstrom, 1977;

83 Preisendorfer and Mobley, 1986). Some schemes depend only on the solar zenith angle while

84 others additionally depend on quantities like wind speed or cloud optical depth, inducing

85 substantial differences in OSA patterns and variability. Li et al. (2006) investigated the impact

86 of various OSA schemes in the Canadian atmosphere climate model, AGCM4. The

87 authors show that the difference in clear-sky upwelling shortwave radiation between schemes

88 can reach 20 W m^{-2} at the top-of-the-atmosphere and more than 20 W m^{-2} at the surface.

89

90 Most of the schemes assessed in Li et al. (2006) do not resolve spectral variations in OSA

91 thus excluding the possibility to represent subtle processes and couplings in Earth system

92 models. Indeed, changes in whitecaps and ocean color, whether due to climate variability or

93 climate change, can modify the OSA, with potential impacts on photochemistry in the

94 atmosphere and biological activity in the upper-most layer of the ocean (Hense et al., 2017).

95

96 In this study, we propose a new interactive OSA scheme well-adapted for the current

97 generation of Earth system models which may benefit from and benefit to the coupling

98   between earth system model components like surface ocean wave or marine biogeochemistry.

99   This study provides details of its implementation into two atmospheric models and discusses

100   its performance on daily to seasonal time scales.

101

102   The outline is as follows. In Section 2, we introduce the formulation of the interactive OSA

103   scheme which is based on old schemes published in literature over the last decades. In Section

104   3, we analyze the importance of the various components of this scheme. Assessment of the

105   simulated OSA in two atmosphere models in comparison to available observations is detailed

106   in Section 4. Section 5 concludes the present study.

107

108   **2- Interactive Ocean Surface Albedo parameterization**

109   Albedo is a measure of the reflectivity of a surface and is defined as the fraction of the

110   incident solar radiation that is reflected by the surface. It depends not only on the properties of

111   the surface but also on the properties of the solar radiation incident on that surface.

112   Technically-speaking albedo can be computed from the knowledge of the spectral and

113   directional distribution of the incident solar radiation $L(\lambda,\theta,\varphi)$ and the bidirectional

114   reflectance distribution function (BRDF), $\rho(\lambda,\theta_i,\varphi_i,\theta_r,\varphi_r)$ which links the reflected radiation in

115   a direction (θ_r,φ_r) to that of incident radiation in a direction (θ_i,φ_i). Here, λ represents the

116   wavelength, and (θ,φ) the zenith and azimuthal angles.

117   While the atmospheric incident radiation, $L(\lambda,\theta,\varphi)$, can be solved using a radiative transfer

118   model and the BRDF can be modelled from the knowledge of the surface ocean properties,

119   the complexity and the computational cost of such models are prohibitive for climate

120   applications. Thus, estimation of OSA in climate models has to rely on several simplifying

121   assumptions. In particular, incident solar radiation is usually characterized by a downward

122   direct flux (for which SZA is known) and a diffuse downward flux (for which a typical

123   angular distribution can be assumed).

124   In the present work, most of the analytic formulations employed are derived from the

125   azimuthally averaged radiative transfer equation (Chandrasekhar, 1960), enabling a

126   straightforward estimation of the OSA for direct and diffuse radiation. This implies that zenith

127   solar angle is the only directional parameter involved in the parametrization.

128

129   The suite of processes involved in our scheme is displayed in Figure 1. The incident solar

130   radiation (either direct or diffuse) is first influenced by the presence of foam (composing the

131   whitecaps), which exhibits different reflective properties from sea-water. Then, the reflective

132   properties of the uncapped fraction of the sea surface are determined separately for direct and

133   diffuse incident radiation. Finally, the subsurface —or below-water— reflectance of sea water

134   is computed for both direct and diffuse incident radiation.

135

136   Hereafter, we describe the various components of OSA according to the nature of the incident

137   solar radiation (direct or diffuse) and the processes involved in its reflection.

138

139   **2-1 Treatment of whitecaps**

140   The first contribution to the new interactive OSA scheme is the whitecap cover. Indeed, the

141   whitecap albedo, $\alpha_{WC}(\lambda)$, could significantly increase the OSA at high wind speeds (e.g.,

142   Frouin et al., 2001; 1996; Gordon and Wang, 1994; Stramska, 2003).

143   The presence of whitecaps originates from turbulence induced by the breaking of waves,

144   which generates foam at the sea surface (Deane and Stokes, 2002; Melville and Matusov,

145   2002). In the absence of an ocean wave model such as WAM (e.g., Aouf et al., 2006; Ardhuin

146   et al., 2010) which would provide a more accurate whitecap coverage (WC) based on wave

147   significant height (Bell et al., 2013; Woolf, 2005), we used the formulation of WC published

148   in Salisbury et al. (2014). Their expression is based on recent space-borne observations with a

149   37 GHz channel radar. It parametrizes WC as a function of the 10-meter wind speed, w, in

150   unit of m s^{-1}:

151    $WC(w) = 3.97 \, 10^{-2} \, w^{1.59}$

152   As mentioned in Salisbury et al. (2014), this approximation of WC is valid for w ranging

153   between 2 and 20 m s^{-1}, which corresponds well to the range of w values simulated by the

154   current generation of Earth system models. The formulation employed here does not account

155   for temperature dependence of wave-breaking in agreement with other parameterizations for

156   WC (Stramska, 2003) because its effect is weaker than that of surface winds on the whitecaps

157   coverage.

158   In order to solve the spectral dependence of the whitecap albedo, we use the relationship

159   proposed by Whitlock et al. (1982). Yet, we rely on previous work indicating that the

160   whitecap albedo of ordinary foam, $\alpha_{WC}(\lambda)$, tends to be twice lower than that of fresh and

161   dense foam (Koepke, 1984). We consequently apply a ½ coefficient to the formulation

162   proposed by (Whitlock et al., 1982) for $\alpha_{WC}(\lambda)$ from 400 to 2400 nm, as follows:

Geoscientific
Model Development
Discussions

163 $\alpha_{WC}(\lambda)$

164 $= \frac{1}{2} \times \frac{1}{100} (60.063 - 5.127 \ln r_{WC}(\lambda) + 2.779(\ln r_{WC}(\lambda))^2 - 0.713(\ln r_{WC}(\lambda))^3$

165 $+ 0.044(\ln r_{WC}(\lambda))^4)$

166 where r_{WC} is the absorption coefficient of clear water in m^{-1}. We use $r_{WC}(\lambda)$ as published in

167 Whitlock et al. (1982) from 400 to 2400 nm. Outside the 400 to 2400 nm range, we chose to

168 set $r_{WC}(\lambda)$ to zero due to the lack of available data in the literature. Tabulated values of

169 $\alpha_{WC}(\lambda)$ computed using this assumption are provided in Table S1.

170 In the present scheme, we assume that whitecaps reflect equally direct and diffuse incoming

171 solar radiation. We also assume that our formulation, which is based on observations, is not

172 affected by the small contribution from the subsurface reflectance.

173

174

175 **2-2 Treatment of the uncapped surface**

176 **2-2-1 Fresnel surface albedo for direct radiation**

177 We describe the contribution of Fresnel reflection at the ocean surface, which is a major

178 component of the OSA. Fresnel reflection is assumed to depend at a given wavelength, λ, on

179 the solar zenith angle, θ and the refractive index of sea water (n), and the two-dimensional

180 distribution of the ocean surface slopes, f. As mentioned earlier we neglect the dependence

181 on the azimuthal angle of the incident radiation.

182 We follow Jin et al. (2001) and express the direct surface albedo (α_{dir}^S) as follows:

183

184 $\alpha_{dir}^S(\lambda, \theta, w) = r_f(n(\lambda), \mu) - \dfrac{r_f(n(\lambda), \mu)}{r_f(n_0, \mu)} f(\mu, \sigma)$

185

186 where $\mu = \cos(\theta)$, n is the spectral refractive index of sea water, r_f is the Fresnel reflectance

187 for a flat surface and f is a function that accounts for the distribution of multiple reflective

188 facets at the ocean surface. Tabulated values for $n(\lambda)$ are indicated in Table S1. $n_0 = 1.34$

189 corresponds to the refractive index of sea water averaged from 300n to 700 nm (i.e., visible

190 spectrum) for which the f function is estimated.

191

192 The interaction of incident shortwave radiation with the multiple reflective facets at the ocean

193 surface of various angle and direction is difficult to model. It is nonetheless possible to

194 represent statistically the distribution of slope of ocean reflective facets with a probabilistic

195 function. The probabilistic function provided by Cox and Munk (1954) assumes a Gaussian

196 distribution of mean slope facet as follows:

197 $p(tan\vartheta) = \dfrac{1}{\pi\sigma^2} \exp(\dfrac{-tan^2\vartheta}{\sigma^2})$

198 where ϑ is the facet angle, i.e., the angle between the normal to the facet and the normal to the

199 horizontal ocean surface and σ the width the distribution of the facet angle. The parameter σ,

200 also called the surface roughness, is modulated by the influence of surface (i.e. 10-meter)

201 wind speed (w) as $\sigma^2 = 0.003 + 0.00512\,w$. The formulation by Cox and Munk (1954)

202 assume that (1) shading influence of ocean facets is neglected and (2) ocean surfaces never

203 behave as a theoretical Fresnel surface (requiring $\sigma = 0$). These approximations can impact

204 α_{dir}^{S} calculation at high SZA and/or in absence of winds. Besides, this formulation (based on

205 wind speed only) ignores the effect of the wind direction on the wind sea and the effect of

206 swell which both affect the distribution of slopes. This latter set of assumptions can also be

207 revised in the foreseeable future when climate models will include an interactive ocean wave

208 model.

209 In order to account for various impacts of multiple ocean surface facets to α_{dir}^{S} including both

210 multiple scattering (increasing surface reflection) and shading effect (reducing reflection), Jin

211 et al. (2011) have proposed to express f as a polynomial function. This function intends to

212 parameterize the mean contribution of multiple reflective facets at the ocean surface to α_{dir}^{S}

213 using only the parameters μ and σ. This polynomial function is expressed as:

214 $f(\mu,\sigma)$

215 $= (0.0152 - 1.7873\mu + 6.8972\mu^2 - 8.5778\mu^3 + 4.071\sigma - 7.6446\mu\sigma) \times \exp(0.1643$

216 $- 7.8409\mu - 3.5639\mu^2 - 2.3588\sigma + 10.054\mu\sigma)$

217 Coefficients of f have been fitted using several accurate calculations of α_{dir}^{S} using a radiative

218 transfer model (Jin et al., 2006; 2005).

219

220 **2-2-2 Fresnel surface albedo for diffuse radiation**

221 The amount and distribution of incident diffuse radiation strongly depend on the amount and

222 characteristics of cloud and aerosols. It is therefore difficult to derive an analytical

223 formulation for α_{dif}^{S} from a BRDF that would be applicable to all atmospheric conditions. We

224 therefore choose to use the simple expression for the diffuse surface albedo (α_{dif}^{S}) under

225 cloudy sky proposed in Jin et al. (2011) which is:

226 $\alpha_{dif}^{S}(\lambda, w) = -0.1479 + 0.1502\,n(\lambda) - 0.0176\,n(\lambda)\sigma$

Geoscientific
Model Development
Discussions

227 with σ and *n* defined as previously.

228

229 **2-3 Below-water albedo**

230 In this section, we describe the contribution of the below-water albedo α^W to the ocean

231 surface albedo. It is caused by solar radiation penetrating the ocean but eventually returning to

232 the atmosphere after multiple reflections within the sea water volume. Below the ocean

233 surface, solar radiation interacts not only with sea water but also with material in suspension

234 in the water like the marine biological pigment or detrital organic materials (DOM). While

235 previous studies show that DOM can influence radiative properties of the open ocean (e.g.,

236 Behrenfeld and Falkowski, 1997; Dutkiewicz et al., 2015; Kim et al., 2015), we chose to

237 solely account for the influence of the marine biological pigment which is characterized by its

238 chlorophyll content because this has the largest impact at the global scale. Furthermore the

239 abundance of chlorophyll in sea water is monitored from space since decades (e.g.,

240 Behrenfeld et al., 2001; Siegel et al., 2002; Yoder et al., 1993) by so-called ocean color

241 measurements. Such observations can provide a climatology to use in the climate model in

242 absence of ocean biogeochemical module.

243

244 Over the uncapped ocean surface, the fraction of direct radiation penetrating into the upper-

245 most layer of the ocean $1 - \alpha^S_{dir}$ interacts with the sea-water, which has a reflectance R_0.

246 Upwelling radiation can be reflected downward at the air-sea interface with a reflectance r_w.

247 Therefore, the contribution of multiple reflections of the penetrating radiation to the ocean

248 albedo takes the form of the following Taylor series:

249 $\alpha^W(\lambda, \theta, Chl) = (1 - \alpha^S_{dir})(1 - r_w)R_0(1 + r_w R_0 + (r_w R_0)^2 + (r_w R_0)^3 + \cdots)$

250 which can be arranged as follows:

251 $\alpha^W(\lambda, \theta, Chl) = \dfrac{(1 - r_w)R_0}{1 - r_w R_0}(1 - \alpha^S_{dir})$

252 We employ the formulation of r_w and R_0 proposed by Morel and Gentili (1991).

253 These authors express r_w as function of surface roughness σ, that is : $r_w = 0.4817 -$

254 $0.0149\sigma - 0.2070\sigma^2$

255 R_0 represents an apparent optical property of sea water, which can be written as follows:

256 $R_0(\lambda, \eta, \mu, Chl) = \beta(\eta, \mu)\dfrac{0.5 b_w(\lambda) + b_{bp}(\lambda, Chl)}{a_w(\lambda) + a_{bp}(\lambda, Chl)}$

Geoscientific
Model Development
Discussions

257   where $a_w(\lambda)$ and $b_w(\lambda)$ are the absorption and backscattering coefficients of sea water (in m⁻

258   ¹); $a_{bp}(\lambda, Chl)$ and $b_{bp}(\lambda, Chl)$ are absorption and backscattering coefficients of biological

259   pigments (i.e., the chlorophyll).

260    $\beta(\eta, \mu)$ is function of sea water and biological pigment backscattering and can be written as:

261    $\beta(\eta, \mu) = 0.6270 - 0.2227\eta - 0.0513\eta^2 + (0.2465\eta - 0.3119)\mu$

262   where $\mu = \cos(\theta)$ and $\eta = \frac{0.5 b_w(\lambda)}{0.5 b_{w(\lambda)} + b_{bp(\lambda, Chl)}}$.

263   Backscattering of biological pigment, b_{bp}, is computed using the formulation proposed in

264   Morel and Maritorena (2001) which uses chlorophyll concentration, $[Chl]$, as a surrogate of

265   biological pigment concentration as follows:

266    $b_{bp}(\lambda) = 0.416[Chl]^{0.766}(0.002 + \frac{1}{100}(0.50 - 0.25\ln[Chl])\left(\frac{\lambda}{550}\right)^{0.5(\ln[Chl]-0.3)})$

267   with λ expressed here in nm and $[Chl]$ in mg m⁻³. This formulation is valid for $[Chl]$ ranging

268   between 0.02 and 2 mg m⁻³.

269   The absorption of biological pigment, $a_{bp}(\lambda, Chl)$, is also computed using Morel and

270   Maritorena (2001) formalism:

271    $a_{bp}(\lambda) = 0.06\, a_{chl}(\lambda)[Chl]^{0.65} + 0.2(0.00635 + 0.06[Chl]^{0.65})e^{0.014*(440-\lambda)}$

272   where $a_{chl}(\lambda)$ is the absorption of chlorophyll in m⁻¹ and λ and $[Chl]$ as previously defined.

273

274   Previous estimates of $a_{chl}(\lambda)$, $a_w(\lambda)$ and $b_w(\lambda)$ used in by Morel and Maritorena (2001)

275   cover values for wavelengths ranging between 300 to 700 nm. Therefore, we have combined

276   and interpolated several sets of tables of coefficients in order to solve consistently α^W, α^S_{dir}

277   and α^S_{dif} across the same range of wavelengths (i.e., from 200 to 4000 nm). $a_w(\lambda)$ has been

278   derived from tables provided by Smith (1982) and Irvine and Pollack (1968), which spans 200

279   to 800 nm and 800 to 4000 nm, respectively. $a_{chl}(\lambda)$ has been derived from values published

280   in Frigaard et al. (1996) which differ from those in Morel and Maritorena (2001) (Figure 2).

281    $b_w(\lambda)$ is estimated from sea water backscattering coefficients published in (Morel and

282   Maritorena, 2001) that have been interpolated from 300 to 700 nm to 200 to 4000 nm with

283   polynomial splines. Tabulated values for $a_{chl}(\lambda)$, $a_w(\lambda)$ and $b_w(\lambda)$ are given in Table S1.

284

285

286   The difference between direct and diffuse below-water albedo essentially stems from the

287   incident direction of incoming radiation. In the case of direct below-water albedo, α^W_{dir}, μ

288    $= \cos(\theta)$ whereas in the case of diffuse below-water albedo, α_{dif}^{W}, $\mu = 0.676$. This value is

289   considered as an effective angle of incoming radiation of 47.47° according to Morel and

290   Gentili (1991). Hence $\alpha_{dif}^{W}(\lambda, Chl) = \alpha_{dir}^{W}(\lambda, \arccos(0.676), Chl)$.

291

292   **2-5 Computation of OSA**

293   With the various components of OSA being now parameterized, the OSA for direct and

294   diffuse radiation are estimated as follows:

295    $OSA_{dir}(\lambda, \theta, w, Chl) = \left(\alpha_{dir}^{S}(\lambda, \theta, w) + \alpha_{dir}^{W}(\lambda, \theta, Chl)\right)\left(1 - WC(w)\right) + WC(w)\alpha_{WC}(\lambda)$

296    $OSA_{dif}(\lambda, \theta, w, Chl) = \left(\alpha_{dif}^{S}(\lambda, w) + \alpha_{dif}^{W}(\lambda, Chl)\right)\left(1 - WC(w)\right) + WC(w)\alpha_{WC}(\lambda)$

297

298   Since detailed atmospheric radiative transfer (e.g., Clough et al., 2005; Mlawer et al., 1997)

299   are now part of current generation of Earth system models, most of radiative codes resolve

300   radiation from near-ultraviolet (~200 nm) to near-infrared (~4000 nm) wavelengths. Here, we

301   design our scheme to compute both the spectral and broadband OSA. To this effect, the

302   scheme computes the OSA from $\lambda_1 = 200$ to $\lambda_2 = 4000$ nm with a resolution of 10 nm. The

303   contribution of each wavelength interval $d\lambda$ to OSA is weighted by its amount of solar

304   energy under the standard solar spectra ASTM E-490 AM0 (Shanmugam and Ahn, 2007),

305    $E(\lambda)$ assumption as follows.

306    $OSA(\theta, w, Chl) = \int_{\lambda_1=200}^{\lambda_2=4000} E(\lambda) OSA(\lambda, \theta, w, Chl)\, d\lambda \Bigg/ \int_{\lambda_1=200}^{\lambda_2=4000} E(\lambda)\, d\lambda$

307

308   Tabulated values for $E(\lambda)$ are given in Table S1.

309   Finally for the total incoming radiation, the OSA can be written as:

310    $OSA(\theta, w, Chl) = (F_{dir} OSA_{dir}(\theta, w, Chl) + F_{dif} OSA_{dif}(\theta, w, Chl))/(F_{dir} + F_{dif})$

311   where F_{dir} and F_{dif} are the downward surface fluxes of direct and diffuse radiation,

312   respectively. $OSA(\theta, w, Chl)$ is then computed for each model ocean grid cell at each model

313   time-step. it should be noted that the SZA used in LMDZ is the average of the SZA during the

314   daytime fraction of the time step.

315

316   **3 Contribution of various OSA components**

317   In this section, we analyze the geographical structure of OSA which is decomposed as

318   follows:

Geoscientific
Model Development
Discussions

319 $\quad A_{dir}(\theta, w, Chl) = \int_{\lambda_1=200}^{\lambda_2=4000} E(\lambda)(\alpha_{dir}^S(\lambda, \theta, w) + \alpha_{dir}^W(\lambda, \theta, Chl))\, d\lambda \left/ \int_{\lambda_1=200}^{\lambda_2=4000} E(\lambda)\, d\lambda \right.$

320 $\quad A_{dif}(\theta, w, Chl) = \int_{\lambda_1=200}^{\lambda_2=4000} E(\lambda)(\alpha_{dif}^S(\lambda, \theta, w) + \alpha_{dif}^W(\lambda, Chl))\, d\lambda \left/ \int_{\lambda_1=200}^{\lambda_2=4000} E(\lambda)\, d\lambda \right.$

321 $\quad A_{WC} = \int_{\lambda_1=200}^{\lambda_2=4000} E(\lambda)\alpha_{WC}(\lambda)\, d\lambda \left/ \int_{\lambda_1=200}^{\lambda_2=4000} E(\lambda)\, d\lambda = 0.174 \right.$

322

323 where A_{dir} and A_{dif} are the broadband ocean surface albedos for direct and diffuse radiation

324 in the absence of whitecaps albedo; and A_{wc} is the broadband albedo of whitecaps.

325 A_{dir}, A_{dif} and A_{wc} have been estimated from offline calculations using Era-Interim forcing

326 fields from 2000 to 2009 at monthly frequency (Dee et al., 2011) and chlorophyll climatology

327 from SeaWiFS (Siegel et al., 2002). Compared to A_{dir} and A_{dif}, A_{wc} is constant in space;

328 therefore its geographical structure arises from whitecaps coverage (WC).

329

330 Figure 3a show that A_{dir} displays a strong meridional gradient with high values over high

331 latitude oceans and low values over the tropical oceans. It confirms that the solar zenith angle

332 is the prominent drivers of A_{dir}. This albedo exhibits nonetheless geographical structure over

333 the tropical oceans which are linked to the easterlies wind regimes which suggest that surface

334 winds variability may imprint a small but noticeable influence on the ocean surface albedo for

335 direct radiation.

336

337 Compared to A_{dir}, A_{dif} does not exhibit such a large meridional gradient (Figures 3b). A_{dif}

338 shows values close to 0.06. It displays nonetheless values > 0.06 over the subtropical gyres

339 and values < 6% over the North Atlantic and the Southern Ocean in response to the 10 m

340 wind speeds. Those patterns are related to surface winds pattern but also to the geographical

341 structure of oligotrophic gyres with low chlorophyll values enhancing below-water

342 reflectance of diffuse radiation.

343

344 Figures 3c provides further insight on the regional influence of WC which display a

345 broadband albedo of 0.174. Offline calculation of WC shows that whitecaps influence albedo

346 for direct and diffuse radiation where westerly winds blow regularly, that is i.e. in the

Geoscientific
Model Development
Discussions

347   Southern Ocean, the North Atlantic and the North Pacific. A weaker but noticeable influence

348   is also found over the tropical oceans.

349   While A_{wc} is larger than A_{dir} and A_{dif}, the convolution of broadband albedo of the whitecaps

350   and their coverage results in maximal contribution of 0.003 to the broadband albedos for

351   direct and diffuse radiation. Yet, its strong albedo makes the whitecaps an important player at

352   interannual and climate timescales. Indeed, this component of OSA for direct and diffuse

353   radiation is subject to respond to the interannual variability of 10 m wind speed and also to

354   climate change. Indeed, the contraction of Southern Ocean westerly winds (e.g., Boening et

355   al., 2008) might induce subtle regional fluctuations in OSA that can feedback on the climate

356   response.

357

358

359   **4 Materials and methods**

360   **4-1 Observations**

361   To assess model reliability to simulate realistic OSA, we compare fields to available

362   observations. For those observations, we estimate the time-averaged OSA from the ratio

363   between the time-averaged upwelling and downwelling shortwave radiative fluxes provided

364   in those datasets.

365

366   At local scale, we use the CERES Ocean Validation Experiment (COVE, (Rutledge et al.,

367   2006)) ground-based measurements. This instrument ocean platform located at Chesapeake

368   bay provides continuous measurements of several radiative fluxes since 2001. In this study,

369   we use measurements of upwelling and downwelling global (i.e., direct and diffuse)

370   shortwave radiation averaged across several instruments

371   (https://cove.larc.nasa.gov/instruments.html).

372

373   At global scale, we perform model evaluation with retrievals from the CERES satellite

374   radiation measurements (Wielicki et al., 1996). CERES data provides estimates of global

375   shortwave radiation at top of the atmosphere and at the surface. In the present study, we focus

376   on surface estimates since our analyses aims at assessing the representation of ocean surface

377   albedo.

378

379

380   **4-2 Models**

381   **4-2-1 LMDZ**

382   LMDZ is an atmospheric general circulation model developed at the Laboratoire de

383   Météorologie Dynamique. The version of this atmosphere model, so-called LMDZ5A, is

384   described in detail in Hourdin et al. (2013) ; it is part of the main IPSL climate model used for

385   CMIP5 and described in Dufresne et al. (2013) (IPSL-CM5A). The atmospheric resolution is

386   96x95 on the horizontal and 39 layers on the vertical. The old OSA scheme in this version of

387   LMDZ is based on the formulation of Larsen and Barkstrom (1977). It is parameterized in

388   terms of μ as follows:

389    $\alpha_{dir}^{S}(\theta) = \dfrac{0.058}{\mu + 0.30}$

390   Consequently, OSA varies between 0.0446 for a sun at zenith and 0.193 for a sun at the

391   horizon. Direct and diffuse radiation are not distinguished and only a broadband albedo is

392   used in the visible spectrum ($\alpha_{dif}^{S} = \alpha_{dir}^{S}$).

393   In LMDZ, the partitioning between direct and diffuse light is derived from the presence of

394   cloud in the atmosphere model grid-cell.

395

396   We assess simulated OSA using an atmosphere-only simulation with prescribed radiative

397   forcing (greenhouse gases, aerosols, land-cover change) and fixed sea-surface temperature as

398   recommended by CMIP5 (Taylor et al., 2011). LMDZ has been integrated from 1979 up to

399   2012 under this protocol.

400   Similarly to the observations, simulated OSA at a given frequency is derived from ratio

401   between the time-averaged upwelling and downwelling shortwave radiative fluxes at that

402   frequency.

403

404   **4-2-2 ARPEGE-Climat**

405   ARPEGE-Climat v6.1 derives from ARPEGE-Integrated Forecasting System (IFS), the

406   operational numerical weather forecast models of Météo-France and the European Centre for

407   Medium-Range Weather Forecasts (ECMWF). Compared to version used in (Voldoire et al.,

408   2013), several improvements in atmospheric physics have been implemented. They consist in

409   a new vertical diffusion scheme which solves a prognostic turbulent kinetic energy equation

410   following Cuxart et al. (2000), an updated prognostic microphysics representing the specific

411   masses of cloud liquid and ice water, rain and snow, as detailed in Lopez (2002), and a new

412   convection scheme known as the Prognostic Condensates Microphysics Transport PCMT

413 (Guérémy, 2011; Piriou et al., 2007). ARPEGE-Climat v6.1 is implicitly coupled to the

414 surface model called SURFEX (Masson et al., 2013), which considers a diversity of surface

415 formulations for the evolution of four types of surface: land, town, inland water and ocean.

416 The old OSA formulation implemented in SURFEX follows Taylor et al. (1996). This scheme

417 enables the computation of α_{dir}^S as a function of μ:

418 $$\alpha_{dir}^S(\theta) = \frac{0.037}{1.1\mu^{1.4} + 0.15}$$

419 Since this schema does not enable computation of α_{dif}^S, α_{dif}^S is set to a constant value of

420 0.066.

421 Like LMDZ, the partitioning of direct and diffuse radiation depends on the cloud cover in the

422 atmospheric model grid-cell.

423

424 Simulations performed with ARPEGE-Climat also consists in an AMIP simulations as

425 LMDZ, except for sea-surface temperature which relies on data recommended by CMIP6

426 (Eyring et al., 2016a). This simulation also spans from 1979 up to 2012.

427 Analyses are complemented using another simulation of ARPEGE-Climat in which the

428 resolved dynamics is nudged towards that of Era-Interim. Nudging consists in restoring the

429 model wind divergence and vorticity and the surface pressure towards those from Era-Interim.

430 The restoring timescale is 12 hours for the wind divergence and surface pressure and 6 hours

431 for the wind vorticity. This simulation is employed hereafter as a kind of reference of what

432 could be expected by the OSA parameterization if the wind spatio-temporal properties were

433 "realistic". In this case, only the direct-to-diffuse incident radiation partitioning remains tied

434 to ARPEGE-Climat. This simulation replicates the chronology of the observed day-to-day

435 variability of 10m wind speed and hence is expected to be closer to the ground-based

436 observations.

437 For those models simulations, simulated OSA at a given frequency is diagnosed from ratio

438 between the time-averaged upwelling and downwelling shortwave radiative fluxes at that

439 frequency.

440

441

442 **5 Comparison of analytical calculation**

443 In order to better understand changes in simulated OSA, we compare first analytical solution

444 of old and new interactive OSA schemes used in the two atmospheric models for both direct

445 and diffuse radiation (Figure 4).

14

446   Figure 4a shows that old OSA schemes for direct radiation differ in term of response to solar

447   zenith angle. Indeed, for a given solar zenith angle, the scheme used in LMDZ (Larsen and

448   Barkstrom, 1977) leads to a greater OSA than that used in ARPEGE-Climat (Taylor et al.,

449   1996). The shape of the response to variations in solar zenith angle suggests that the scheme

450   used in ARPEGE-Climat leads to a slightly stronger meridional gradient in OSA than that

451   used in LMDZ.

452   Interestingly, the new scheme produces OSA values bracketed by those of old algorithms,

453   except for small solar zenith angle. Under this condition, the effect of winds is to increase

454   OSA up to 0.072. It also displays a greater response to variations in solar zenith angle which

455   differs substantially from those given by the old schemes.

456

457   Differences in OSA for diffuse radiation presented in Figure 4b are noticeable. They clearly

458   illustrate modelling assumptions in the old schemes. Indeed, old schemes have been built on

459   *ad hoc* formulations. Neither Taylor et al. (1996) nor Larsen and Barkstrom (1977) have

460   provided a differentiated OSA for direct and diffuse radiation. This is why OSA for diffuse

461   radiation is set to 0.06 (corresponding to the angular average of the OSA for direct radiation)

462   in ARPEGE-Climat, whereas that of LMDZ is equal to the OSA for direct radiation from

463   Larsen and Barkstrom (1977).

464   Figure 4b shows that the new interactive scheme displays feature similar to the diffuse OSA

465   used in ARPEGE-Climat. This scheme produces nonetheless slightly larger values which can

466   fluctuate in response to other drivers. The old OSA for diffuse radiation employed in LMDZ

467   responds to variations in solar zenith angle while it should not. Errors related to this erroneous

468   representation of OSA for diffuse radiation is also modulated by the partitioning between

469   direct and diffuse radiation estimated by the atmospheric model.

470

471   **6 Evaluation at COVE station (36.905°N, 75.713°W)**

472   In this section, we employ COVE daily data to assess the simulated OSA by both atmospheric

473   models at local scale. OSA is computed here as the ratio of averaged radiation fluxes at daily

474   resolution for both ground-based observations and models. Such an evaluation is fundamental

475   because it relies on direct ground-truth observations over the ocean surface and hence

476   provides a more accurate assessment of the OSA scheme as compared to the global-scale

477   satellite-derived estimates developed in the following sections.

478

479   Figure 5 shows how well model using old and new interactive OSA scheme behaves at daily

480   frequency compared to the ground-based observations at COVE station from 2001 to 2009.

481   Figure 5 and Figure S1a clearly shows that both old OSA schemes of ARPEGE-Climat or

482   LMDZ fail at replicating day-to-day OSA variations at the COVE station. Comparatively,

483   Figure 5 and Figure S1b emphasizes how much the new interactive scheme improves OSA as

484   simulated by both atmospheric models. Indeed, the simulated OSA are now consistent with

485   observation at COVE station, with temporal correlation greater than 0.3. However, the models

486   fail at replicating the large OSA values occurring during the winter in ground-based

487   observations.

488

489   Those findings are reinforced when we compare the probability density function (pdf)

490   estimated from daily-mean OSA as simulated by models against that derived from ground-

491   based observations (Figure 6). This analysis provides further insight on how old and new

492   interactive OSA schemes behave at COVE station. Figure 6 confirms that old schemes fail at

493   capturing the day-to-day variations in OSA. Indeed, day-to-day variations in OSA estimated

494   from old schemes arise from day-to-day variations in SZA and to a lesser extent to variations

495   in direct-to-diffuse ratio of incident radiation which are related to the cloud cover. As shown

496   in Figure 4, old OSA schemes crudely represent diffuse albedo. Therefore, errors in direct-to-

497   diffuse ratio of incident radiation imprint errors in the simulated OSA. Consequently, day-to-

498   day variations are better reproduced when the albedo for diffuse radiation is realistically

499   simulated (Figure 6). In particular, the new interactive scheme captures the minimum OSA

500   values occurring during the summer which are lower than 0.06.

501

502

503   At seasonal scale, OSA estimated from averaged radiative fluxes agrees with the above-

504   mentioned findings for ground-based observations and models. Figure 7 clearly demonstrates

505   that old OSA schemes are unable to capture seasonal variations of observed OSA. Correlation

506   between observation-derived OSA and that simulated by both models is 0.32 for ARPEGE-

507   Climat and 0.28 for LMDZ is very low, indicating an unrealistic representation of OSA. This

508   erroneous representation of OSA at seasonal scale leads, at least for this location, to a

509   systematic bias in the surface energy budget of +3 W m^{-2} in winter and -1.5 W m^{-2} in summer.

510   Figure 7 shows significant improvements in the simulated OSA in both models using the new

511   interactive scheme. In both models, the simulated seasonal cycle of OSA replicates the

512   minimum observed during the summer. However, models do not capture large values of OSA

513   of 0.10 occurring during the winter. That said, model-data comparison shows that correlation

514   with observations has been improved. Indeed, correlation between observed and simulated

515   daily values over a mean yearly cycle has increased from 0.23 to 0.84 in LMDZ to 0.32 to

516   0.86 in ARPEGE-Climat.

517

518

519   Although improved, Figures 5, 6 and 7 show that new interactive OSA scheme seems to

520   suffer from a systematic bias in winter and miss OSA values greater than 0.10. This is

521   supported by the fact that this systematic bias is displayed for all model estimates

522   independently from the atmospheric physics and dynamics (i.e., LMDZ, ARPEGE-Climat and

523   nudged OSA). That being said, some other possible reasons can explain such deviations

524   between models and ground-based data. First, current atmosphere models suffer from

525   systematic errors in the ratio of direct-to-diffuse radiation which can be related to bias in

526   cloud cover or aerosol optical thickness (as shown in Figure S2). A larger-than-observed

527   atmospheric optical depth in winter may favor diffuse path with the respect to the direct path,

528   resulting in a lower-than-observed OSA Second, coarse resolution atmospheric models are not

529   able to replicate the mesoscale meteorological and oceanic conditions at this very location.

530   Differences in surface wind between the models and field conditions can increase the

531   contribution of whitecaps albedo with the respect to that of the Fresnel reflectance. Third,

532   local ocean conditions and the presence of ocean waves resulting from remoted wind

533   influence (i.e., swell) are not simulated by the atmospheric models. This would lead to an

534   underestimate of the contributions of both whitecaps and Fresnel reflectance.

535

536   **7 Global-scale evaluation**

537   **7-1 Climatological mean**

538   This section is dedicated to evaluate OSA at global-scale using global satellite product that

539   are routinely used in Earth system models evaluation (Eyring et al., 2016b; Gleckler et al.,

540   2008). We thus use OSA retrieved from CERES surface product to assess the simulated OSA

541   by ARPEGE-Climat and LMDZ.

542   Figure 8 presents geographical pattern of OSA as simulated by ARPEGE-Climat and LMDZ

543   using Taylor et al. (1996) and Larsen and Barkstrom (1977) schemes, respectively. These old

544   OSA schemes were used during CMIP5 and thus give an idea of errors in the models'

545   radiative budgets.

Geoscientific
Model Development
Discussions

546 Globally, the simulated OSA overestimates the CERES-derived estimate (~0.058) by about

547 0.007. Yet, the most striking feature is the substantial differences in the meridional structure.

548 CERES-derived OSA shows maximum values over the high-latitudes oceans and minimum

549 values over the tropical oceans. None of the models using old schemes are able to capture this

550 meridional structure. Deviations are particularly high for LMDZ, which hardly replicates

551 maximum OSA over high-latitude oceans and minimum OSA over tropical oceans. Both

552 models exhibit poor spatial correlation with -0.03 for LMDZ and 0.40 for ARPEGE-Climat.

553 Model-data errors in OSA mirror model bias in surface upwelling shortwave radiation, which

554 amounts to ~7 W m^{-2} over the tropical oceans compared to CERES.

555 The new interactive scheme improves favorably the comparison with observations (Figure 8).

556 Indeed global mean OSA is equal to 0.062 for LMDZ and 0.057 for ARPEGE-Climat, which

557 better matches the value derived from CERES data. As such, the model bias in surface

558 upwelling shortwave radiation has been reduced by ~1 W m^{-2} in average over the ocean and

559 by up to ~5 W m^{-2} over the tropical oceans.

560 Both models capture the meridional structure of the OSA with spatial correlations of about

561 0.82 for LMDZ and 0.86 for ARPEGE-Climat. Nonetheless, the simulated OSA displays

562 some biases. In LMDZ and ARPEGE-Climat, the modeled OSA over the North Atlantic is

563 slightly overestimated and shifted to the South. Major differences between simulated OSA are

564 noticeable over the tropical oceans, where models differ in terms of zonal structure. LMDZ

565 displays OSA of ~0.06 over Eastern boundary upwelling systems, which is slightly too high

566 compared to CERES. Differences in the OSA geographical structure between ARPEGE-

567 Climat and LMDZ arise from differences in 10-meter wind speed (Figure S3) and direct-to-

568 diffuse incident radiation as diagnosed from the simulated cloud cover (Figure S4). Large-

569 scale deviations between models and observations seem to be related to differences in 10-

570 meter wind fields (Figure S3). Model-data deviations in OSA at the regional scale rather

571 mirror biases in total cloud cover (Figure S4). This is especially clear over low-latitude oceans

572 where LMDZ overestimate OSA over the eastern boundary upwelling systems where LMDZ

573 overestimates the cloud cover (Figure S4). This result is expected since over the low-latitude

574 oceans the contribution of diffuse OSA is stronger than that of direct OSA (Figures 3 and 4).

575

576 **7-2 Seasonal variability**

577 Figure 9 compares the simulated and CERES-derived OSA on the seasonal scale. This time

578 scale matters for modelling accurately the Earth's climate because the flow of incoming

Geoscientific
Model Development
Discussions

579   radiation fluctuates up to one order of magnitude between winter and summer at high

580   latitudes.

581   Figure 9abc shows that both models using old OSA schemes hardly reproduce the seasonal

582   cycle of OSA derived from CERES. This is particularly the case for LMDZ, which produced

583   an unrealistic seasonal cycle for OSA. LMDZ fails at simulating maximum OSA during the

584   winter of both hemispheres. Instead, extreme values of simulated OSA occur at 50°N and

585   50°S during the summer. Simulated OSA in ARPEGE-Climat does not present these features

586   but is biased high at all seasons.

587   With the new interactive scheme, the seasonal OSA is improved in both models (Figure 9de).

588   The simulated OSA matches that derived from CERES at seasonal scale, with high values

589   during the winter and low values between 30°S and 30°N. Improvement is especially

590   noticeable for LMDZ which captures the observed seasonal cycle of OSA.

591   However, a few errors remain in the simulated OSA. In LMDZ, OSA is slightly too high

592   compared to CERES (~0.002) in boreal and austral summer. Nonetheless, simulated OSA

593   reproduces realistic OSA values in the tropics (~5.2%). In ARPEGE-Climat, instead, the

594   simulated OSA seems slightly too low compared to CERES (~-0.002). This leads ARPEGE-

595   Climat to overestimate the fraction of low-OSA ocean. Interestingly this bias solely concerns

596   the tropical oceans. Indeed, simulated OSA over high-latitude oceans displays realistic

597   features at the seasonal scale. The fact that errors in ARPEGE-Climat and LMDZ are of

598   different signs tends to suggest that the new interactive scheme is not intrinsically biased. It

599   rather points to biases in driving fields such as the surface wind speeds or the ratio between

600   direct and diffuse shortwave radiation simulated by either ARPEGE-Climat or LMDZ (Figure

601   S2).

602

603

604   **8- Conclusions**

605   In this paper, we have detailed a new interactive scheme for ocean surface albedo suited for

606   Earth system models. This scheme computes the ocean surface albedo accounting for the

607   spectral dependence (across a range of wavelengths between 200 and 4000 nm), the

608   characteristics of incident solar radiation (direct of diffuse), the effects of surface winds,

609   chlorophyll content and whitecaps in addition to the canonical solar zenith angle dependence.

610   This scheme enables a better coupling between the atmospheric and oceanic components of

611   the model. It thus provides a much more physical basis to resolve the radiative transfer at the

612   interface between the atmosphere and the upper ocean. This work can be extended to include

Geoscientific
Model Development
Discussions

613 a coupling to an ocean wave model that would provide a more realistic distribution of ocean

614 surface state.

615

616 Although direct and diffuse albedos were included in the old ocean albedo schemes of the two

617 atmospheric models used here, our results demonstrate that their assumptions employed for

618 diffuse albedo (i.e., fixed values or equal to the direct albedo) are not realistic. The new

619 interactive scheme improves its representation which leads to substantially reduce model-data

620 error in ocean surface albedo over the low-latitude oceans.

621

622 Comparison to available dataset shows, for at least two state-of-the-art climate models, a

623 noticeable improvement in terms of simulated ocean surface albedo compared to their old

624 ocean surface albedo schemes. At the global scale, geographical pattern of simulated ocean

625 surface albedo has been improved in both models. The simulated seasonal cycle also shows a

626 noticeable improvement, especially in LMDZ, with a better correlation to CERES data (up to

627 0.8). At the local scale, simulated ocean surface albedo also fits ocean surface albedo derived

628 from ground-based radiative measurements at daily resolution with an improved correlation

629 up to 0.8.

630

631 Compared to old schemes, the new interactive scheme is more complex and induces a slight

632 increase in model elapsed time of about 2%. Although noticeable, this increase does not

633 preclude centennial-long simulation or high resolution model simulations.

634

635 Improved ocean surface albedo might lead to difference in the simulated climate or marine

636 biogeochemistry dynamics which will be assessed in future work. Indeed, a difference of

637 about 1% of simulated ocean surface albedo for a global mean irradiance of ~180 W m^{-2} can

638 induce a deviation in energy flow of the Earth system comparable to the impact of land-cover

639 changes over land (Myhre et al., 2013).

640

641

642 **Code availability:**

643 The interactive ocean surface albedo code detailed in the paper is a part of the SURFEX

644 ocean scheme and is available as open source via http://www.cnrm-game-meteo.fr/surfex/.

645 SURFEX is updated at a relatively low frequency (every 3 to 6 months) and the developments

646 presented in this paper are available starting from SURFEX version 8.0. The LMDZ

Geoscientific
Model Development
Discussions

647   implementation is available as part of the LMDZ code which can be downloaded at

648   http://LMDZ.lmd.jussieu.fr/. Besides, all the tabulated values use for this algorithm are

649   available in the supplementary materials.

650

660

661

662   **References:**

663   Allen, M. R., Frame, D. J., Huntingford, C., Jones, C. D., Lowe, J. A., Meinshausen, M. and
664   Meinshausen, N.: Warming caused by cumulative carbon emissions towards the trillionth
665   tonne, Nature, 458(7242), 1163–1166, doi:10.1038/nature08019, 2009.

666   Aouf, L., Lefevre, J.-M. and Hauser, D.: Assimilation of Directional Wave Spectra in the
667   Wave Model WAM: An Impact Study from Synthetic Observations in Preparation for the
668   SWIMSAT Satellite Mission, J. Atmos. Oceanic Technol., 23(3), 448–463,
669   doi:10.1175/JTECH1861.1, 2006.

670   Ardhuin, F., Rogers, E., Babanin, A. V., Filipot, J.-F., Magne, R., Roland, A., van der
671   Westhuysen, A., Queffeulou, P., Lefevre, J.-M., Aouf, L. and Collard, F.: Semiempirical
672   Dissipation Source Functions for Ocean Waves. Part I: Definition, Calibration, and
673   Validation, J. Phys. Oceanogr., 40(9), 1917–1941, doi:10.1175/2010JPO4324.1, 2010.

674   Behrenfeld, M. J. and Falkowski, P. G.: Photosynthetic rates derived from satellite-based
675   chlorophyll concentration, Limnology and Oceanography, 42(1), 1–20 [online] Available
676   from: http://www.es.ucsc.edu/~rkudela/OS130/OS130_1116A.PDF, 1997.

677   Behrenfeld, M. J., Randerson, J. T., McClain, C. R., Feldman, G. C., Los, S. O., Tucker, C. J.,
678   Falkowski, P. G., Field, C. B., Frouin, R., Esaias, W. E., Kolber, D. D. and Pollack, N. H.:
679   Biospheric Primary Production During an ENSO Transition, Science, 291(5513), 2594–2597,
680   doi:10.1126/science.1055071, 2001.

681   Bell, T. G., De Bruyn, W., Miller, S. D., Ward, B., Christensen, K. and Saltzman, E. S.: Air–
682   sea dimethylsulfide (DMS) gas transfer in the North Atlantic: evidence for limited interfacial
683   gas exchange at high wind speed, Atmos. Chem. Phys., 13(21), 11073–11087,

684   doi:10.5194/acp-13-11073-2013, 2013.

685   Böning, C. W., Dispert, A., Visbeck, M., Rintoul, S. R. and Schwarzkopf, F. U.: The response
686   of the Antarctic Circumpolar Current to recent climate change, *Nature Geoscience*, *1*(12),
687   864–869, doi:10.1038/ngeo362, 2008.
688
689   Chandrasekhar, S.: Radiative heat transfer, Dover Publications, New York, 11, 11–12, 1960.

690   Chepfer, H., Bony, S., Winker, D., Cesana, G., Dufresne, J.-L., Minnis, P., Stubenrauch, C. J.
691   and Zeng, S.: The GCM-Oriented CALIPSO Cloud Product (CALIPSO-GOCCP), J.
692   Geophys. Res., 15, D00H16, doi:10.1029/2009JD012251, 2010.
693
694   Clough, S. A., Shephard, M. W., Mlawer, E. J., Delamere, J. S., Iacono, M. J., Cady-Pereira,
695   K., Boukabara, S. and Brown, P. D.: Atmospheric radiative transfer modeling: a summary of
696   the AER codes, Journal of Quantitative Spectroscopy and Radiative Transfer, 91(2), 233–244,
697   2005.

698   Cox, C. and Munk, W.: Measurement of the Roughness of the Sea Surface from Photographs
699   of the Sun's Glitter, J. Opt. Soc. Am., 44(11), 838–850, 1954.

700   Cuxart, J., Bougeault, P. and Redelsperger, J. L.: A turbulence scheme allowing for mesoscale
701   and large-eddy simulations, Q.J.R. Meteorol. Soc., 126(562), 1–30,
702   doi:10.1002/qj.49712656202, 2000.

703   Deane, G. B. and Stokes, M. D.: Scale dependence of bubble creation mechanisms in
704   breaking waves, Nature, 418(6900), 839–844, doi:10.1038/nature00967, 2002.

705   Dee, D. P., Uppala, S. M., Simmons, A. J., Berrisford, P., Poli, P., Kobayashi, S., Andrae, U.,
706   Balmaseda, M. A., Balsamo, G., Bauer, P., Bechtold, P., Beljaars, A. C. M., van de Berg, L.,
707   Bidlot, J., Bormann, N., Delsol, C., Dragani, R., Fuentes, M., Geer, A. J., Haimberger, L.,
708   Healy, S. B., Hersbach, H., Hólm, E. V., Isaksen, L., Kållberg, P., Köhler, M., Matricardi, M.,
709   McNally, A. P., Monge-Sanz, B. M., Morcrette, J. J., Park, B. K., Peubey, C., de Rosnay, P.,
710   Tavolato, C., Thépaut, J. N. and Vitart, F.: The ERA-Interim reanalysis: configuration and
711   performance of the data assimilation system, Q.J.R. Meteorol. Soc., 137(656), 553–597, 2011.

712   Dufresne, J.-L., Foujols, M. A., Denvil, S., Caubel, A., Marti, O., Aumont, O., Balkanski, Y.,
713   Bekki, S., Bellenger, H., Benshila, R., Bony, S., Bopp, L., Braconnot, P., Brockmann, P.,
714   Cadule, P., Cheruy, F., Codron, F., Cozic, A., Cugnet, D., Noblet, N., Duvel, J. P., Ethe, C.,
715   Fairhead, L., Fichefet, T., Flavoni, S., Friedlingstein, P., Grandpeix, J. Y., Guez, L.,
716   Guilyardi, E., Hauglustaine, D., Hourdin, F., Idelkadi, A., Ghattas, J., Joussaume, S.,
717   Kageyama, M., Krinner, G., Labetoulle, S., Lahellec, A., Lefebvre, M.-P., Lefèvre, F., Lévy,
718   C., Li, Z. X., Lloyd, J., Lott, F., Madec, G., Mancip, M., Marchand, M., Masson, S.,
719   Meurdesoif, Y., Mignot, J., Musat, I., Parouty, S., Polcher, J., Rio, C., Schulz, M.,
720   Swingedouw, D., Szopa, S., Talandier, C., Terray, P., Viovy, N. and Vuichard, N.: Climate
721   change projections using the IPSL-CM5 Earth System Model: from CMIP3 to CMIP5, Clim
722   Dyn, 40(9-10), 2123–2165, doi:10.1007/s00382-012-1636-1, 2013.

723   Dutkiewicz, S., Hickman, A. E., Jahn, O., Gregg, W. W., Mouw, C. B. and Follows, M. J.:
724   Capturing optically important constituents and properties in a marine biogeochemical and
725   ecosystem model, Biogeosciences Discuss., 12(3), 2607–2695, doi:10.5194/bgd-12-2607-
726   2015, 2015.

Geoscientific
Model Development
Discussions

727 Eyring, V., Bony, S., Meehl, G. A., Senior, C. A., Stevens, B., Stouffer, R. J. and Taylor, K.
728 E.: Overview of the Coupled Model Intercomparison Project Phase 6 (CMIP6) experimental
729 design and organization, Geosci. Model Dev, 9(5), 1937–1958, doi:10.5194/gmd-9-1937-
730 2016, 2016a.

731 Eyring, V., Gleckler, P. J., Heinze, C., Stouffer, R. J., Taylor, K. E., Balaji, V., Guilyardi, E.,
732 Joussaume, S., Kindermann, S., Lawrence, B. N., Meehl, G. A., Righi, M. and Williams, D.
733 N.: Towards improved and more routine Earth system model evaluation in CMIP, Earth Syst.
734 Dynam., 7(4), 813–830, doi:10.5194/esd-7-813-2016, 2016b.

735 Frigaard, N.-U., Larsen, K. L. and Cox, R. P. A.: Spectrochromatography of photosynthetic
736 pigments as a fingerprinting technique for microbial phototrophs, FEMS Microbiology
737 Ecology, 20(2), 69–77, doi:10.1111/j.1574-6941.1996.tb00306.x, 1996.

738 Frouin, R., Iacobellis, S. F. and Deschamps, P. Y.: Influence of oceanic whitecaps on the
739 Global Radiation Budget, Geophys. Res. Lett., 28(8), 1523–1526,
740 doi:10.1029/2000GL012657, 2001.

741 Frouin, R., Schwindling, M. and Deschamps, P.-Y.: Spectral reflectance of sea foam in the
742 visible and near-infrared: In situ measurements and remote sensing implications, J. Geophys.
743 Res., 101(C6), 14361–14371, doi:10.1029/96JC00629, 1996.

744 Frölicher, T. L.: Climate response: Strong warming at high emissions, Nature Clim. Change,
745 6(9), 823–824, doi:10.1038/nclimate3053, 2016.

746 Gillett, N. P., Arora, V. K., Matthews, D. and Allen, M. R.: Constraining the Ratio of Global
747 Warming to Cumulative CO2 Emissions Using CMIP5 Simulations*, J. Climate, 26(18),
748 6844–6858, doi:10.1175/JCLI-D-12-00476.s1, 2013.

749 Gleckler, P. J., Taylor, K. E. and Doutriaux, C.: Performance metrics for climate models, J.
750 Geophys. Res., 113(D6), D06104, doi:10.1029/2007JD008972, 2008.

751 Gordon, H. R. and Wang, M.: Influence of oceanic whitecaps on atmospheric correction of
752 ocean-color sensors, Appl. Opt., 33(33), 7754–7763, doi:10.1364/AO.33.007754, 1994.

753 Guérémy, J. F.: A continuous buoyancy based convection scheme: one- and three-
754 dimensional validation, Tellus A, 63(4), 687–706, doi:10.1111/j.1600-0870.2011.00521.x,
755 2011.

756 Gupta, S., Ritchey, N., Wilber, A. and Whitlock, C.: A climatology of surface radiation
757 budget derived from satellite data, J. Climate, 12, 2691–2710, https://doi.org/10.1175/1520-
758 0442(1999)012<2691:ACOSRB>2.0.CO;2, 1999.
759
760 Hansen, J., Russell, G., Rind, D., Stone, P., Lacis, A., Lebedeff, S., Ruedy, R. and Travis, L.:
761 Efficient Three-Dimensional Global Models for Climate Studies: Models I and II, Mon. Wea.
762 Rev., 111(4), 609–662, doi:10.1175/1520-0493(1983)111<0609:ETDGMF>2.0.CO;2, 1983.

763 Hense, I., Stemmler, I. and Sonntag, S.: Ideas and perspectives: climate-relevant marine
764 biologically driven mechanisms in Earth system models, Biogeosciences, 14(2), 403–413,
765 doi:10.5194/bg-14-403-2017, 2017.

766 Hourdin, F., Foujols, M.-A., Codron, F., Guemas, V., Dufresne, J.-L., Bony, S., Denvil, S.,

Geoscientific
Model Development
Discussions

767   Guez, L., Lott, F., Ghattas, J., Braconnot, P., Marti, O., Meurdesoif, Y. and Bopp, L.: Impact
768   of the LMDZ atmospheric grid configuration on the climate and sensitivity of the IPSL-
769   CM5A coupled model, Climate Dynamics, 40(9-10), 2167–2192, doi:10.1007/s00382-012-
770   1411-3, 2013.

771   IPCC, 2001: *Climate Change 2001: The Scientific Basis*, edited by T. J. Houghton, Y. Ding,
772   D. J. Griggs, M. Noguer, P. J. van der Linden, X. Dai, K. Maskell, and C. A. Johnson,
773   Cambridge University Press, Cambridge, United Kingdom and New York, NY, USA. 2001.

774   IPCC, 2007: Climate Change 2007: The Physical Science Basis, edited by S. Solomon, D.
775   Qin, M. Manning, Z. Chen, M. Marquis, K. B. Averyt, M. Tignor, and H. L. Miller,
776   Cambridge University Press, Cambridge, United Kingdom and New York, NY, USA. 2007.

777   IPCC, 2013: Climate Change 2013: The Physical Science Basis., edited by T. F. Stoker, D.
778   Qin, G. Plattner, M. Tignor, S. K. Allen, J. Boschung, A. Nauels, Y. Xia, V. Bex, and P. M.
779   Midgley, Cambridge Univ Press, Cambridge, United Kingdom and New York, NY, USA.
780   2013.

781   Irvine, W. M. and Pollack, J. B.: Infrared optical properties of water and ice spheres, Icarus,
782   8(1), 324–360, 1968.

783   Jin, Z.: A parameterization of ocean surface albedo, Geophys. Res. Lett., 31(22),
784   doi:10.1029/2004GL021180, 2004.

785   Jin, Z., Charlock, T. P. and Rutledge, K.: Analysis of Broadband Solar Radiation and Albedo
786   over the Ocean Surface at COVE, J. Atmos. Oceanic Technol., 19(10), 1585–1601,
787   doi:10.1175/1520-0426(2002)019<1585:AOBSRA>2.0.CO;2, 2002.

788   Jin, Z., Charlock, T. P., Rutledge, K., Cota, G., Kahn, R., Redemann, J., Zhang, T., Rutan, D.
789   A. and Rose, F.: Radiative transfer modeling for the CLAMS experiment, Journal of the
790   atmospheric sciences, 62(4), 1053–1071, 2005.

791   Jin, Z., Charlock, T. P., Rutledge, K., Stamnes, K. and Wang, Y.: Analytical solution of
792   radiative transfer in the coupled atmosphere-ocean system with a rough surface, Appl. Opt.,
793   45(28), 7443–7455, 2006.

794   Jin, Z., Qiao, Y., Wang, Y., Fang, Y. and Yi, W.: A new parameterization of spectral and
795   broadband ocean surface albedo, Optics Express, 19(27), 26429–26443, 2011.

796   Kent, E. C., Forrester, T. N. and Taylor, P. K.: A comparison of oceanic skin effect
797   parameterizations using shipborne radiometer data, J. Geophys. Res., 101(C7), 16649,
798   doi:10.1029/96JC01054, 1996.

799   Kim, G. E., Pradal, M. A. and Gnanadesikan, A.: A new parameterization for surface ocean
800   light attenuation in Earth System Models: assessing the impact of light absorption by colored
801   detrital material, Biogeosciences Discuss., 12(5), 3905–3942, doi:10.5194/bgd-12-3905-2015,
802   2015.

803   Koepke, P.: Effective reflectance of oceanic whitecaps, Appl. Opt., 23(11), 1816–1824,
804   doi:10.1364/AO.23.001816, 1984.

Geoscientific
Model Development
Discussions

805   Larsen, J. C. and Barkstrom, B. R.: Effects of realistic angular reflection laws for the Earth's
806   surface upon calculations of the Earth-atmosphere albedo, Radiation in the Atmosphere,
807   Proceedings of an International Symposium, Princeton: Science Press, p. 451. 1977.
808
809   Li, J., Scinocca, J., Lazare, M., McFarlane, N., Salzen, von, K. and Solheim, L.: Ocean
810   Surface Albedo and Its Impact on Radiation Balance in Climate Models, J. Climate, 19(24),
811   6314–6333, doi:10.1175/JCLI3973.1, 2006.

812   Li, T., Bai, Y., Li, G., He, X., Chen, C.-T., Gao, K. and Liu, D.: Effects of ultraviolet
813   radiation on marine primary production with reference to satellite remote sensing, Front.
814   Earth Sci., 1–11, doi:10.1007/s11707-014-0477-0, 2014.

815   Lopez, P.: Implementation and validation of a new prognostic large-scale cloud and
816   precipitation scheme for climate and data-assimilation purposes, Q.J.R. Meteorol. Soc.,
817   128(579), 229–257, doi:10.1256/00359000260498879, 2002.

818   Masson, V., Le Moigne, P., Martin, E., Faroux, S., Alias, A., Alkama, R., Belamari, S.,
819   Barbu, A., Boone, A., Bouyssel, F., Brousseau, P., Brun, E., Calvet, J.-C., Carrer, D.,
820   Decharme, B., Delire, C., Donier, S., Essaouini, K., Gibelin, A. L., Giordani, H., Habets, F.,
821   Jidane, M., Kerdraon, G., Kourzeneva, E., Lafaysse, M., Lafont, S., Lebeaupin Brossier, C.,
822   Lemonsu, A., Mahfouf, J. F., Marguinaud, P., Mokhtari, M., Morin, S., Pigeon, G., Salgado,
823   R., Seity, Y., Taillefer, F., Tanguy, G., Tulet, P., Vincendon, B., Vionnet, V. and Voldoire,
824   A.: The SURFEXv7.2 land and ocean surface platform for coupled or offline simulation of
825   earth surface variables and fluxes, Geosci. Model Dev, 6(4), 929–960, doi:10.5194/gmd-6-
826   929-2013-supplement, 2013.

827   Melville, W. K. and Matusov, P.: Distribution of breaking waves at the ocean surface, Nature,
828   417(6884), 58–63, doi:10.1038/417058a, 2002.

829   Mlawer, E. J., Taubman, S. J., Brown, P. D., Iacono, M. J. and Clough, S. A.: Radiative
830   transfer for inhomogeneous atmospheres: RRTM, a validated correlated-k model for the
831   longwave, J. Geophys. Res., 102(D14), 16663–16682, doi:10.1029/97JD00237, 1997.

832   Morel, A. and Antoine, D.: Heating rate within the upper ocean in relation to its bio-optical
833   state, J. Phys. Oceanogr., 24(7), 1652–1665, https://doi.org/10.1175/1520-
834   0485(1994)024<1652:HRWTUO>2.0.CO;2, 1994.
835
836   Morel, A. and Gentili, B.: Diffuse reflectance of oceanic waters: its dependence on Sun angle
837   as influenced by the molecular scattering contribution, Appl. Opt., 30(30), 4427–4438,
838   doi:10.1364/AO.30.004427, 1991.

839   Morel, A. and Maritorena, S.: Bio-optical properties of oceanic waters: A reappraisal, Journal
840   of Geophysical Research-Oceans, 1 *106(C4), 7163–7180, doi:10.1029/2000JC000319*, 2001.
841
842   Murtugudde, R., Beauchamp, J. and McClain, C. R.: Effects of penetrative radiation on the
843   upper tropical ocean circulation, J. Climate, **15**, 470–486, https://doi.org/10.1175/1520-
844   0442(2002)015<0470:EOPROT>2.0.CO;2, 2002.
845
846   Myhre, G., Boucher, O., Breon, F.-M., Forster, P. and Shindell, D.: Declining uncertainty in
847   transient climate response as CO2 forcing dominates future climate change, Nature Geosci,
848   8(3), 181–185, doi:10.1038/ngeo2371, 2015.

Geoscientific
Model Development
Discussions

849   Myhre, G., Shindell, D., Breon, F.-M., Collins, W., Fuglestvedt, J., Huang, J., Koch, D.,
850   Lamarque, J.-F., Lee, D., Mendoza, B., Nakajima, T., Robock, A., Stephens, G., Takemura, T.
851   and Zhang, H.: Anthropogenic and Natural Radiative Forcing, Climate Change 2013: The
852   Physical Science Basis. Contribution of Working Group I to the Fifth Assessment Report of
853   the Intergovernmental Panel on Climate Change. 2013.

854   Nelson, D. M. and Smith, W. O. J.: The role of light and major nutrients, Limnol. Oceanogr.,
855   36(8), 1650–1661, 1991.

856   Otto, A., Otto, F. E. L., Boucher, O., Church, J., Hegerl, G., Forster, P. M., Gillett, N. P.,
857   Gregory, J., Johnson, G. C., Knutti, R., Lewis, N., Lohmann, U., Marotzke, J., Myhre, G.,
858   Shindell, D., Stevens, B. and Allen, M. R.: Energy budget constraints on climate response, **6**,
859   415-416, doi:10.1038/ngeo1836, 2013.
860

861   Piriou, J.-M., Redelsperger, J.-L., Geleyn, J.-F., Lafore, J.-P. and Guichard, F.: An Approach
862   for Convective Parameterization with Memory: Separating Microphysics and Transport in
863   Grid-Scale Equations, J. Atmos. Sci., 64(11), 4127–4139, doi:10.1175/2007JAS2144.1, 2007.

864   Preisendorfer, R. W. and Mobley, C. D.: Albedos and Glitter Patterns of a Wind-Roughened
865   Sea Surface, J. Phys. Oceanogr., 16(7), 1293–1316, doi:10.1175/1520-
866   0485(1986)016<1293:AAGPOA>2.0.CO;2, 1986.

867   Rutledge, C. K., Schuster, G. L., Charlock, T. P., Denn, F. M., Smith, W. L., Jr., Fabbri, B. E.,
868   Madigan, J. J., Jr. and Knapp, R. J.: Offshore Radiation Observations for Climate Research at
869   the CERES Ocean Validation Experiment: A New "Laboratory" for Retrieval Algorithm
870   Testing, Bull. Amer. Meteor. Soc., 87(9), 1211–1222, doi:10.1175/BAMS-87-9-1211, 2006.

871   Salisbury, D. J., Anguelova, M. D. and Brooks, I. M.: Global Distribution and Seasonal
872   Dependence of Satellite-based Whitecap Fraction, Geophys. Res. Lett., 2014GL059246,
873   doi:10.1002/2014GL059246, 2014.

874   Shanmugam, P. and Ahn, Y. H.: Reference solar irradiance spectra and consequences of their
875   disparities in remote sensing of the ocean colour, Annales Geophysicae, 25(6), 1235–1252,
876   doi:10.5194/angeo-25-1235-2007, 2007.

877   Siegel, D. A., Doney, S. C. and Yoder, J. A.: The North Atlantic spring phytoplancton bloom
878   and the Sverdrup's critical depth hypothesis, Science, 296, 730–733,
879   doi:10.1126/science.1069174, 2002.

880   Smith, E. D.: Water Characteristics, Journal (Water Pollution Control Federation), 54(6),
881   541–554, 1982.

882   Smyth, T. J.: Penetration of UV irradiance into the global ocean, J. Geophys. Res., 116(C11),
883   C11020, 2011.

884   Stramska, M.: Observations of oceanic whitecaps in the north polar waters of the Atlantic, J.
885   Geophys. Res., 108(C3), 3086, doi:10.1029/2002JC001321, 2003.

886   Taylor, J. P., Edwards, J. M., Glew, M. D., Hignett, P. and Slingo, A.: Studies with a flexible
887   new radiation code. II: Comparisons with aircraft short-wave observations, Q.J.R. Meteorol.
888   Soc., 122(532), 839–861, doi:10.1002/qj.49712253204, 1996.

Geoscientific
Model Development
Discussions

889 Taylor, K. E., Stouffer, R. J. and Meehl, G. A.: An Overview of CMIP5 and the Experiment
890 Design, Bull. Amer. Meteor. Soc., doi:10.1175/BAMS-D-11-00094.1, 2011.

891 Voldoire, A., Sanchez-Gomez, E., Salas y Mélia, D., Decharme, B., Cassou, C., Sénési, S.,
892 Valcke, S., Beau, I., Alias, A., Chevallier, M., Déqué, M., Deshayes, J., Douville, H.,
893 Fernandez, E., Madec, G., Maisonnave, E., Moine, M. P., Planton, S., Saint-Martin, D.,
894 Szopa, S., Tyteca, S., Alkama, R., Belamari, S., Braun, A., Coquart, L. and Chauvin, F.: The
895 CNRM-CM5.1 global climate model: description and basic evaluation, Climate Dynamics,
896 40(9-10), 2091–2121, doi:10.1007/s00382-011-1259-y, 2013.

897 Whitlock, C. H., Bartlett, D. S. and Gurganus, E. A.: Sea foam reflectance and influence on
898 optimum wavelength for remote sensing of ocean aerosols, Geophys. Res. Lett., 9(6), 719–
899 722, doi:10.1029/GL009i006p00719, 1982.

900 Wielicki, B. A., Barkstrom, B. R., Harrison, E. F., Lee, R. B., III, Louis Smith, G. and
901 Cooper, J. E.: Clouds and the Earth's Radiant Energy System (CERES): An Earth Observing
902 System Experiment, Bull. Amer. Meteor. Soc., 77(5), 853–868, doi:10.1175/1520-
903 0477(1996)077<0853:CATERE>2.0.CO;2, 1996.

904 Woolf, D. K.: Effect of wind waves on air–sea gas exchange: proposal of an overall CO_2
905 transfer velocity formula as a function of breaking-wave parameter, Tellus B, 57(2), 478–487,
906 doi:10.1023/A:1021215904955, 2005.

907 Yoder, J., McClain, C., Feldman, G. and Esaias, W.: Annual Cycles of Phytoplankton
908 Chlorophyll Concentrations in the Global Ocean - a Satellite View, Global Biogeochem.
909 Cycles, 7(1), 181–193, *doi:10.1029/93GB02358*, 1993.

910

911

912

913

914

915

916

917

918

919

920

921

922

923

924

925

926
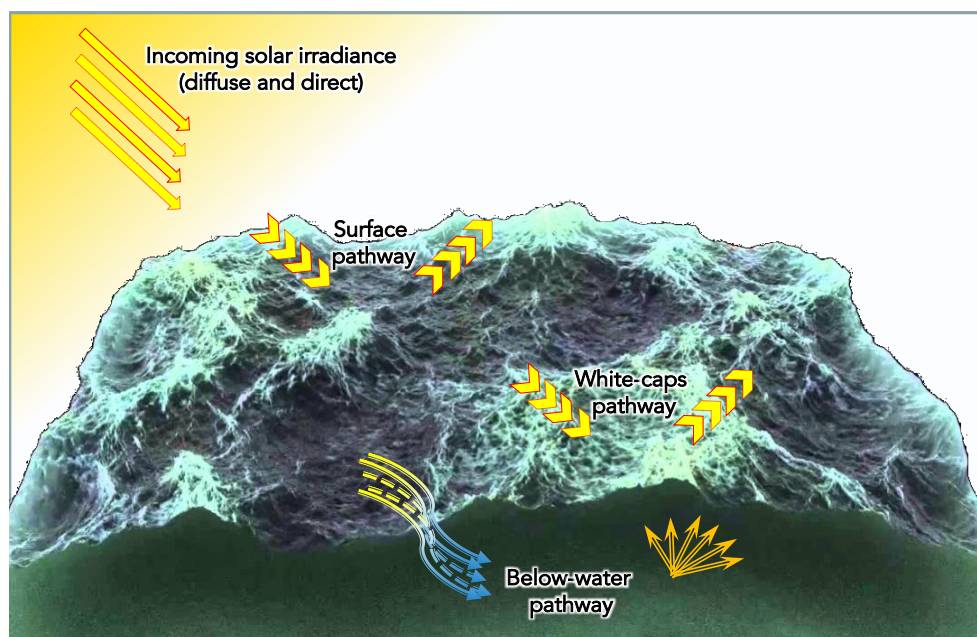
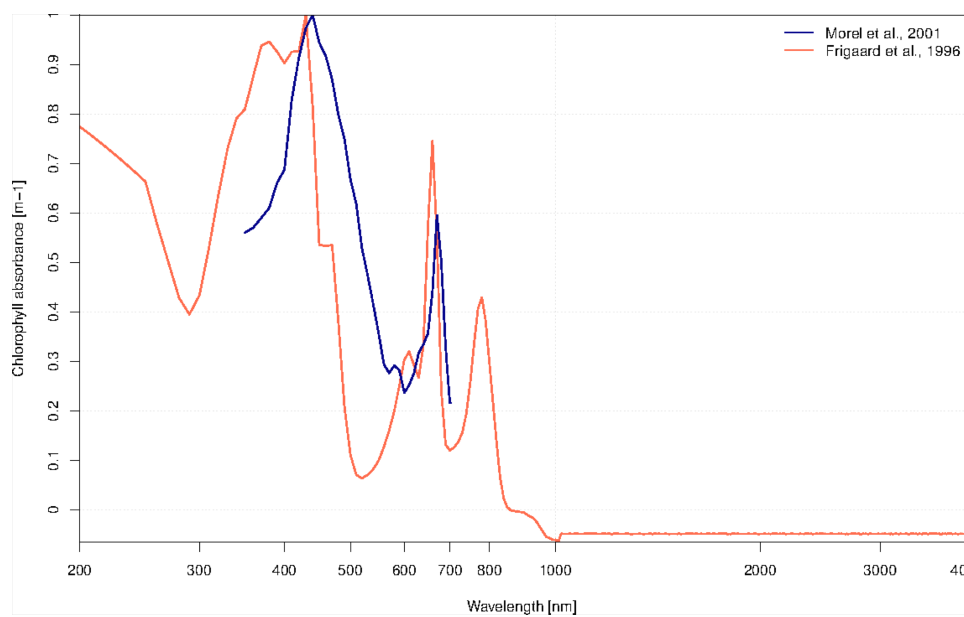**Figure 1**: Pathways of solar radiation over oceans as described in the new interactive scheme. Whitecaps, surface Fresnel or below-water influence of the reflection or the refraction of both direct and diffuse radiation.

930

931

932

933

Geoscientific
Model Development
Discussions

Open Access

EGU

934

Figure 2: Comparison of chlorophyll absorbance (m^{-1}) as a function of wavelength (nm, in log-scale) from Morel and Maritorena (2001) in blue to that of Frigaard et al. (1996) in red, which is used in the new interactive OSA scheme.

935

936

937

938

939

940

941

942

943

944

945

946

947

948

Geoscientific
Model Development
Discussions

949

950

Geoscientific
Model Development
Discussions

951
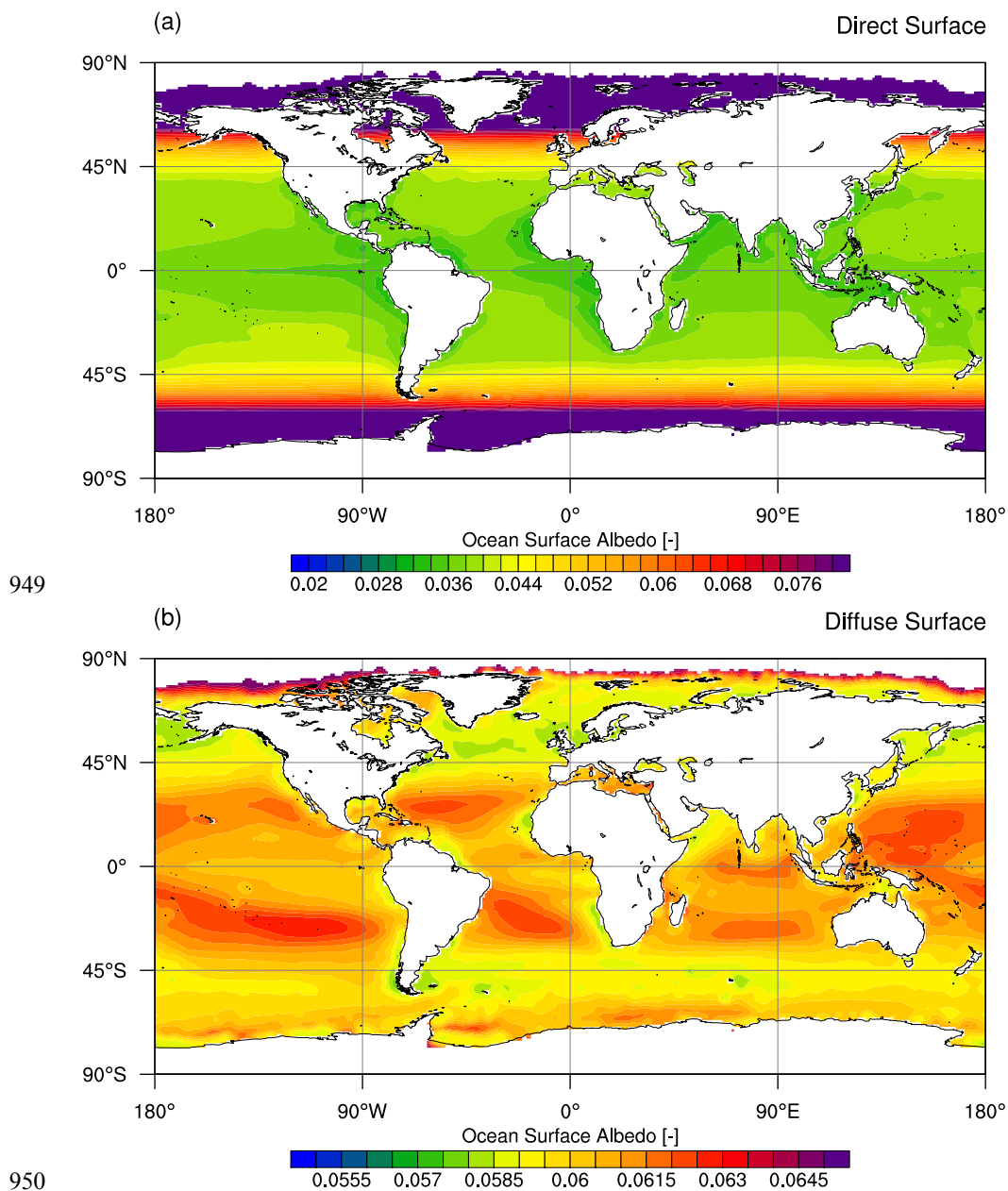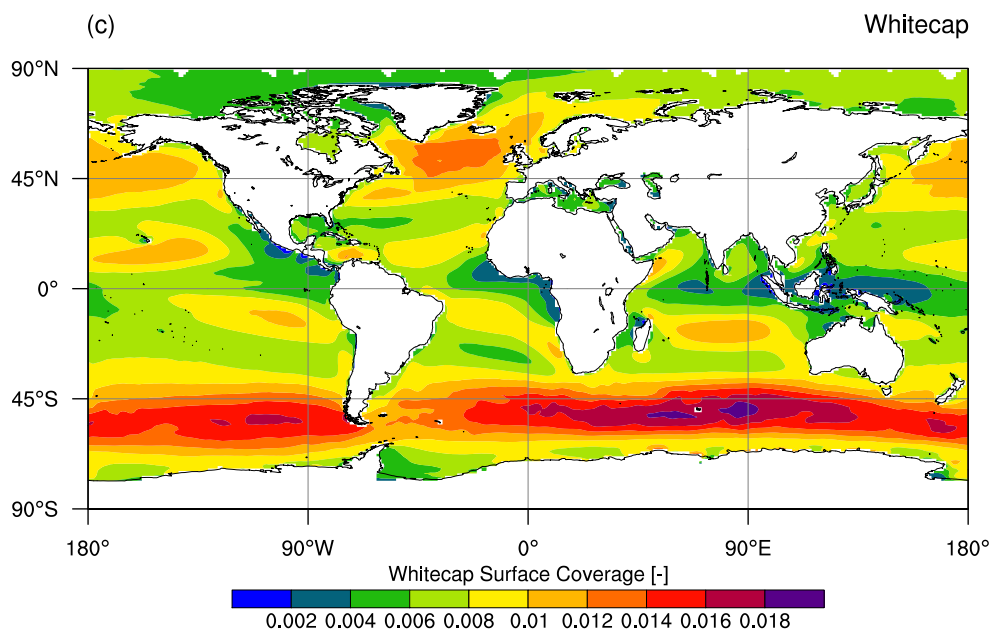
Figure 3: Maps of ocean surface albedo for (a) direct and (b) diffuse radiation in the absence

of whitecaps, and map of whitecaps surface coverage (c). Estimates are derived from offline

calculation using EraInterim forcings fields (Dee et al., 2011) from years 2000 to 2012 and

SeaWiFS chlorophyll climatology (Siegel et al., 2002) over year 1998-2007. Whitecap albedo

is constant in space and is equate to 0.174.

957

958

Geoscientific
Model Development
Discussions
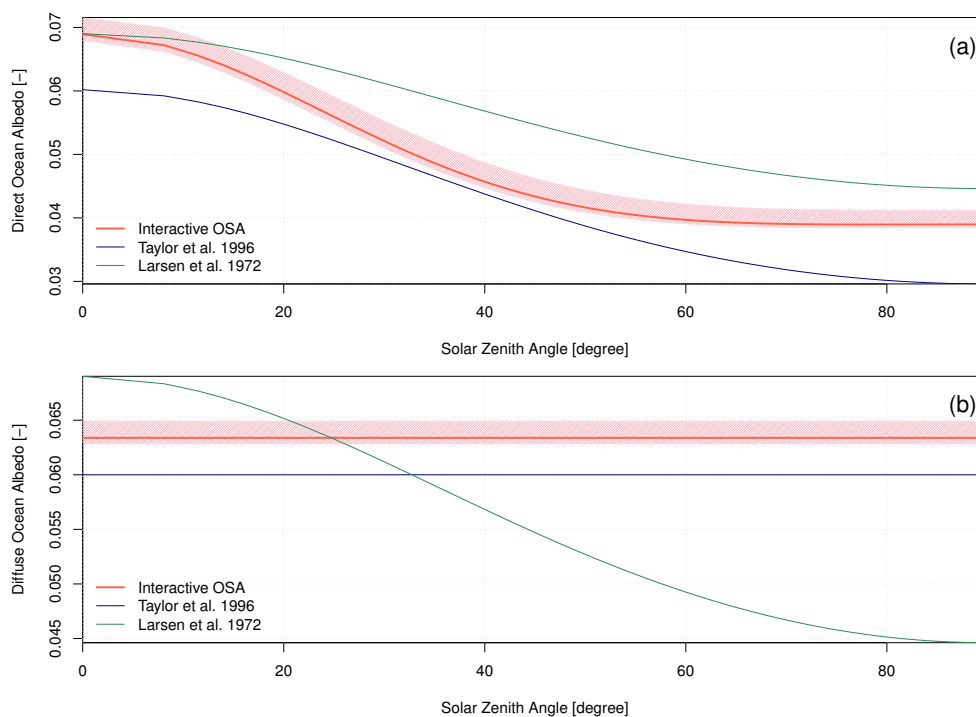
Figure 4: Analytical solution for (a) direct and (b) diffuse ocean surface albedo as used in Taylor et al. (1996) and Larsen and Barkstrom (1977), and computed solution for the new interactive ocean surface albedo scheme, as a function of solar zenith angle. Hatching depicts potential variations related to changes in 10-meter wind speed and surface chlorophyll.
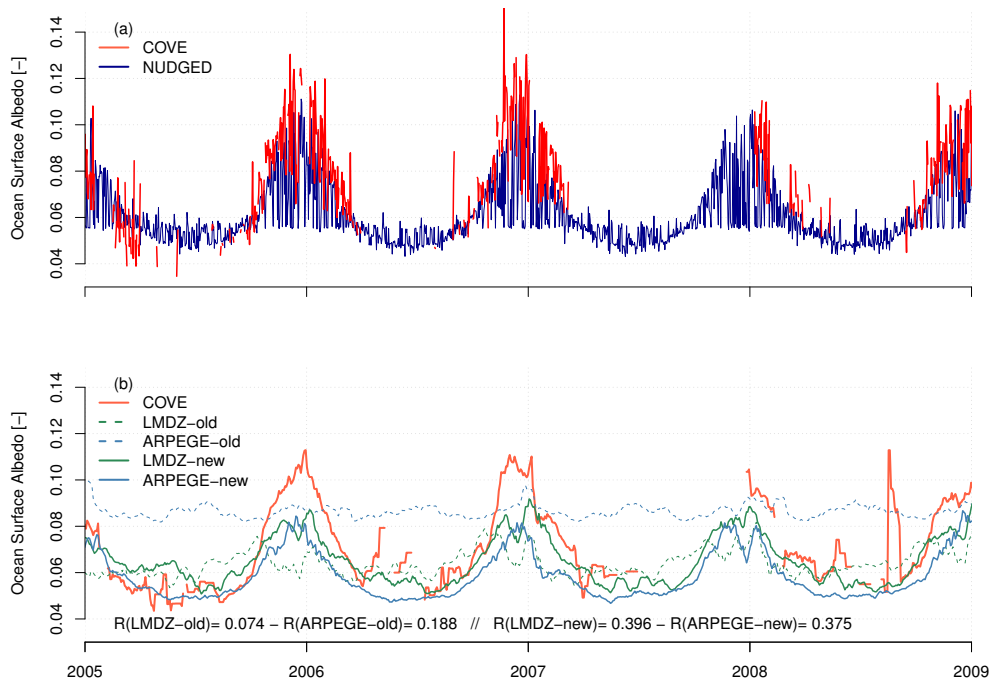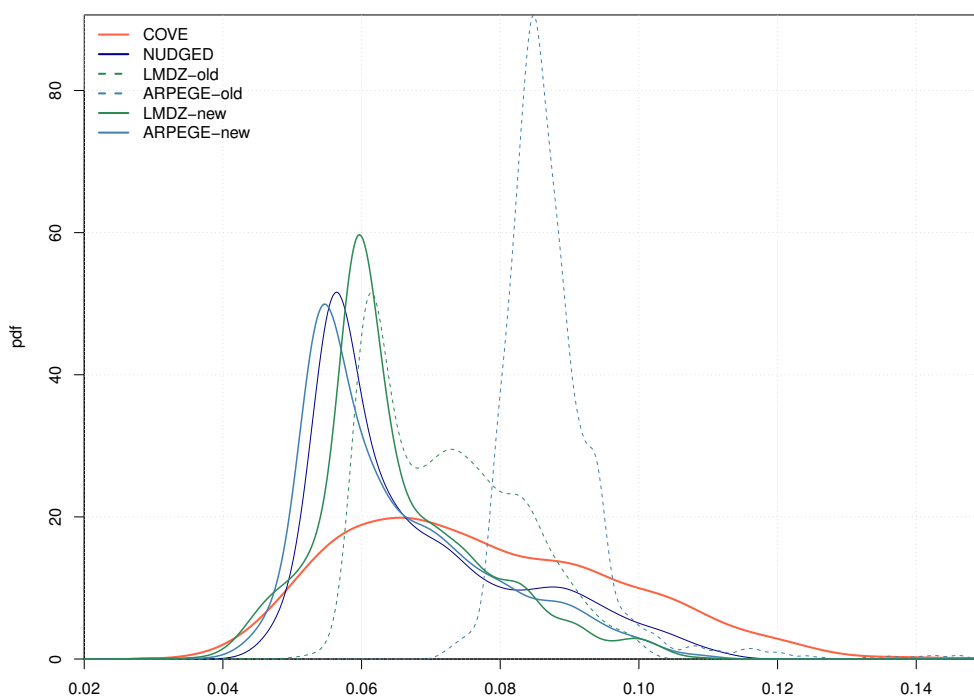
Figure 5: Ocean surface albedo at COVE station (36.905°N, 75.713°W) from 2005 to 2009. Panel (a) compares daily-mean time series of ocean surface albedo as derived from ground-based observations (in red) and as reconstructed with ARPEGE-Climat nudged toward EraInterim (dark blue). Panel (b) displays, for the sake of clarity, time series of daily-mean Ocean surface albedo smoothed using a 5-day moving average for both observations and model results. All daily-mean time-series from 2001 to 2015 are displayed in Figure S1. Ocean surface albedo simulated by ARPEGE-Climat (in blue) and LMDZ (in green) using old or the new interactive scheme are indicated with dashed or solid lines, respectively.

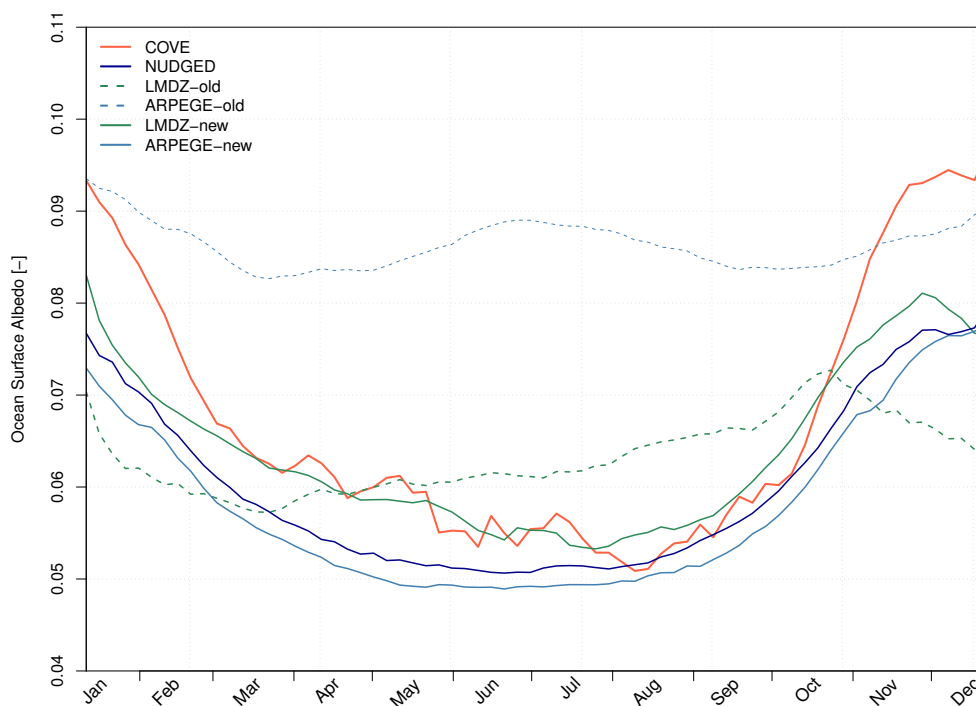**Figure 6**: Probability density function of daily-mean ocean surface albedo at COVE station (36.905°N, 75.713°W) derived from daily-mean time series over years 2001 to 2013. Ocean surface albedo derived from ground-based observations and as reconstructed with ARPEGE-Climat nudged toward EraInterim are indicated in red and dark blue, respectively. Ocean surface albedo simulated by ARPEGE-Climat (in blue) and LMDZ (in green) using old or the new interactive scheme are indicated with dashed or solid lines, respectively.
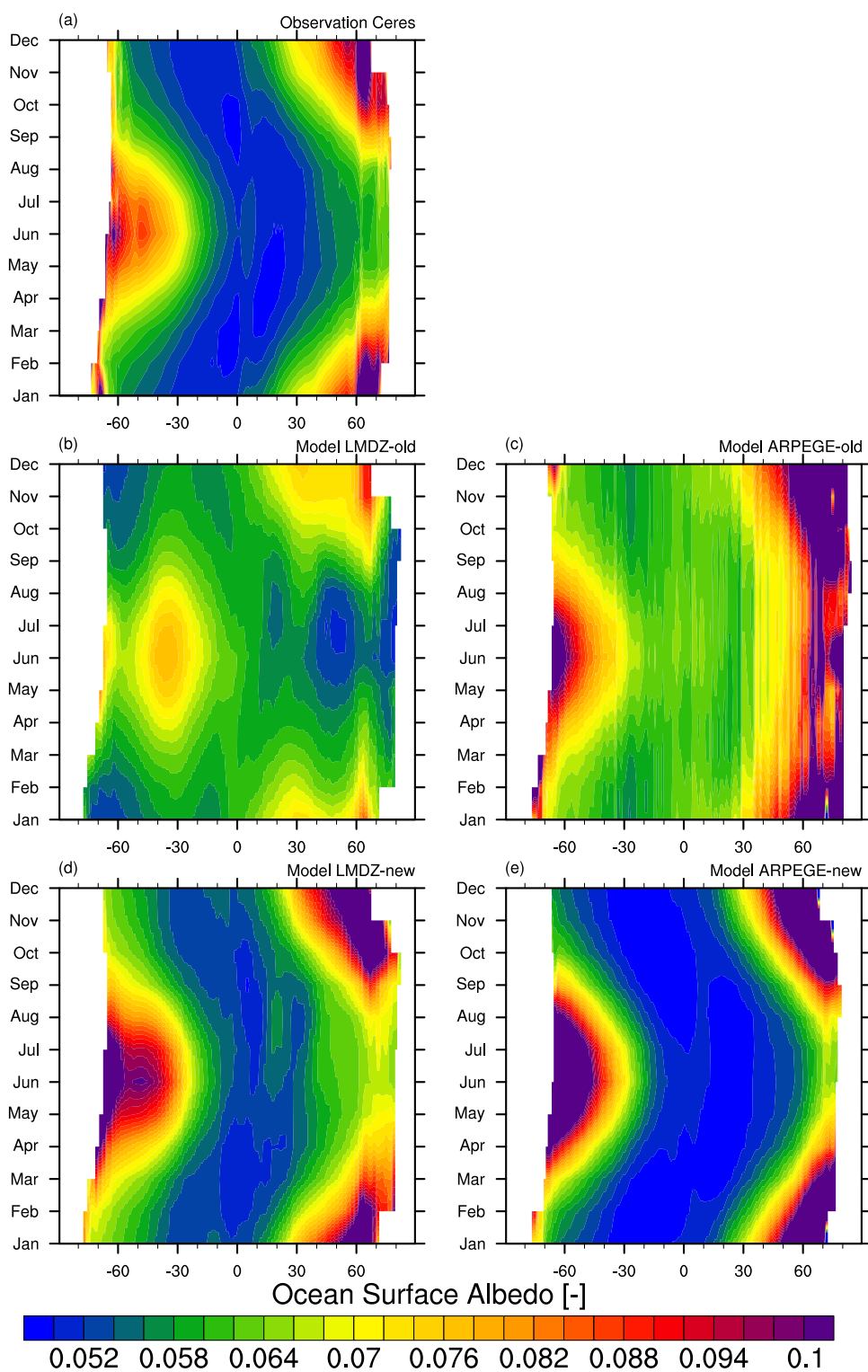
986

Figure 7: Mean seasonal cycle of ocean surface albedo at COVE station (36.905°N, 75.713°W) derived from daily-mean time series over years 2001 to 2013. Ocean surface albedo derived from ground-based observations and as reconstructed with ARPEGE-Climat nudged toward EraInterim are indicated in red and dark blue, respectively. Ocean surface albedo simulated by ARPEGE-Climat (in blue) and LMDZ (in green) using old or the new interactive scheme are indicated with dashed or solid lines, respectively.

993
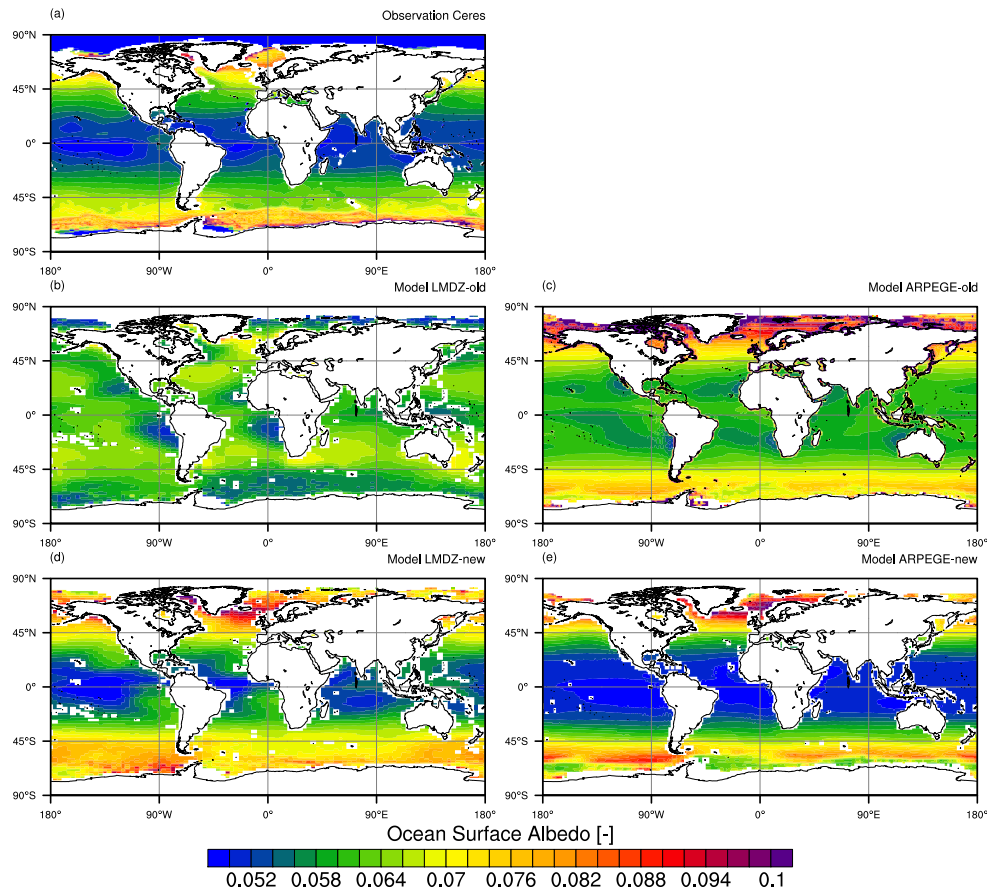
Figure 8: Decadal-mean climatology ocean surface albedo as (a) estimated from CERES satellite observations (Wielicki et al., 1996) and as simulated by LMDZ (b,d) and ARPEGE-Climat (c,e). In panels (b) and (c), LMDZ and ARPEGE-Climat use old ocean albedo schemes, that is Taylor et al. (1996) and Larsen and Barkstrom (1977), respectively. In panels (d) and (e), LMDZ and ARPEGE-Climat use employ the new interactive ocean surface albedo scheme. Decadal-mean climatology is derived from radiative fluxes averaged over years 2001 to 2014 for CERES estimates and 2000 to 2012 for both climates models.

Geoscientific
Model Development
Discussions

Geoscientific
Model Development
Discussions

1004   **Figure 9**: Hovmöller diagram representing the zonally-averaged ocean surface albedo as a

1005   function of month. The various panels display the ocean surface albedo as (a) estimated from

1006   CERES satellite observations (Wielicki et al., 1996) and as simulated by (b) LMDZ and (c)

1007   ARPEGE-Climat using old ocean albedo schemes, that is Taylor et al. (1996) and Larsen and

1008   Barkstrom (1977), respectively. Panels (d) and (e) show OSA as simulated by the new

1009   interactive ocean surface albedo scheme for LMDZ and ARPEGE-Climat, respectively.

1010   Monthly-mean are derived from radiative fluxes averaged over years 2001 to 2014 for

1011   CERES estimates and from years 2000 to 2012 for both climates models.

1012